Magnetic resonance (MR) safety and compatibility of a novel iron bioresorbable scaffold

Dong Bian[a,b,1], Li Qin[a,1], Wenjiao Lin[a], Danni Shen[b], Haiping Qi[a], Xiaoli Shi[c], Gui Zhang[d], Hongwei Liu[e], Han Yang[e], Jin Wang[c], Deyuan Zhang[a,**], Yufeng Zheng[b,*]

[a] Biotyx Medical (Shenzhen) Co.,Ltd, Shenzhen, 518110, Guangdong, China
[b] Department of Materials Science and Engineering, College of Engineering, Peking University, Beijing, 100871, China
[c] Key Lab. of Advanced Technology for Materials of Education Ministry, School of Materials Science and Engineering, Southwest Jiaotong University, Chengdu, 610031, Sichuan, China
[d] Shenzhen Advanced Medical Services Co., Ltd, Shenzhen, 518000, Guangdong, China
[e] Shen Zhen Testing Center of Medical Devices, Shenzhen, 518057, Guangdong, China

ARTICLE INFO

ABSTRACT

Fully bioresorbable scaffolds have been designed to overcome the limitations of traditional drug-eluting stents (DESs), which permanently cage the native vessel wall and pose possible complications. The ultrathin-strut designed sirolimus-eluting iron bioresorbable coronary scaffold system (IBS) shows comparable mechanical properties to traditional DESs and exhibits an adaptive degradation profile during target vessel healing, which makes it a promising candidate in all-comers patient population. For implanted medical devices, magnetic resonance (MR) imaging properties, including MR safety and compatibility, should be evaluated before its clinical use, especially for devices with intrinsic ferromagnetism. In this study, MR safety and compatibility of the IBS scaffold were evaluated based on a series of well-designed in-vitro, ex-vivo and in-vivo experiments, considering possible risks, including scaffold movement, over-heating, image artifact, and possible vessel injury, under typical MR condition. Traditional ASTM standards for MR safety and compatibility evaluation of intravascular devices were referred, but not only limited to that. The unique time-relevant MR properties of bioresorbable scaffolds were also discussed. Possible forces imposed on the scaffold during MR scanning and MR image artifacts gradually decreased along with scaffold degradation/absorption. Rigorous experiments designed based on a scientifically based rationale revealed that the IBS scaffold is MR conditional, though not MR compatible before complete absorption. The methodology used in the present study can give insight into the MR evaluation of magnetic scaffolds (bioresorbable) or stents (permanent).

1. Introduction

1.1. Current status of bioresorbable scaffolds

Despite all the benefits of currently used permanent drug-eluting stents (DESs), concerns have been raised over their long-term safety, especially for the items of very late thrombosis and possible long-term foreign-body responses [1]. To overcome those shortcomings, fully bioresorbable scaffold (BRS) have been developed. BRS can provide scaffolding and anti-restenosis benefits in the short term and then gradually disappear over time to free the vessel [2–4]. A majority of these scaffold are currently still undergoing preclinical or clinical trials, and, only limited ones received market approval in limited application areas [5,6]. The ideal and ultimate goal of BRS is to restore the physiological function of the target vessel to the normal level, at the best case.

Up to now, the BRS can be roughly classified into two categories, i.e. the bioresorbable polymeric scaffold and the bioresorbable metallic scaffold, based on the scaffold backbone materials they used [7,8]. The polymeric group contains polymers of poly-L-lactide (PLLA), poly-D,L-lactide (PDLLA) and desaminotyrosine polycarbonate (PTD-PC). The metallic group contains metals of magnesium (Mg), zinc (Zn), iron (Fe)

and their alloys [6]. Mechanical properties of metallic scaffolds are generally superior to their polymeric counterparts, owning to the inherent properties of metals. So, bioresorbable metallic scaffolds with higher scaffolding force might be used with wider indications, such as calcified arteries and complex cases, compared to bioresorbable polymeric scaffolds.

1.2. Introduction of the investigational device

The sirolimus-eluting iron bioresorbable coronary scaffold system (IBS) developed by Biotyx Medical (Shenzhen) Co., Ltd (Biotyx, Spunoff from Lifetech Scientific Corporation in 2019) is the very first iron-based bioresorbable scaffold worldwide, which has entered into clinical trials both in China and in Malaysia [9], on the basis of a massive preclinical data. This scaffold is basically composed of three parts, i.e. the nitrided iron backbone, a zinc buffer layer (~600 nm) and a sirolimus-eluting polylactic acid coating. The nitrided iron backbone is the framework of the IBS scaffold, and it offers the radial force [10]. A poly-DL-lactide (PDLLA) drug-loaded coating controls the drug release to treat local diseased vessel. Besides, iron corrosion could be accelerated by the hydrolysis of PDLLA that produced soluble monomers consisting of carboxylic acid groups after vessel remodeling [11,12]. The Zn buffer layer protects the nitrided iron backbone from corrosion at the initial stage after implantation by consuming itself, and it determines when the iron corrosion onsets [11]. Finally, corrosion products of iron can be cleared away by macrophages [13]. The perfect integration of those three components makes the degradation profile, drug-releasing curve and mechanical deterioration behavior properly favor the vessel repair and remodeling [11]. More details about the IBS scaffold could be found in our previous publications [10,11,13,14]. The IBS scaffold is a strong competitor to traditional permanent DESs and also to the developing BRS family, as it persists the superior mechanical performance of traditional DESs and also owns the bioresorbable ability of BRS.

1.3. Introduction of magnetic resonance imaging (MRI)

Magnetic resonance imaging (MRI) is a noninvasive imaging technique that produces three-dimensional anatomical images, which could be employed in the diagnosis of many aspects, including the diagnosis of cardiovascular diseases [15,16]. Magnetic resonance (MR) does not pose the danger of exposing patients to ionizing radiation or X-rays, and it basically avoids using nephrotoxic contrast agents. However, MR examination in patient with implanted endovascular devices, especially the metallic ones, is sometimes a risky procedure. During the MR examination, a strong magnetic field is applied, and the magnetic field exerts very powerful forces on ferromagnetic objects. Possible heating

of previously implanted devices in such a magnetic field is also a big concern [17]. Metals with high volume magnetic susceptibility, such as 316L stainless steel and Co–Cr alloy would generate artifacts in the MR image as a result of distortion of the magnetic field [18,19]. During a MR examination, close attention should be paid to deal with patient who has received an implantable device, especially the implant contains ferromagnetic components.

Risks associated with MR scanning generally arise from three aspects considering their distinct mechanisms, i.e. the static main magnetic field, radiofrequency (RF) energy and gradient magnetic field [20]. Currently, clinical MR scanners are typically used under a high intensity magnetic field ranging from 1.5 to 3 T (T), which corresponds to 30000–60000 times the strength of the Earth's magnetic field. A device may be moved, rotated, dislodged, or accelerated in this field due to ferromagnetic interactions. The higher the static magnetic field applied, the greater the resultant ferromagnetic forces would be induced [21]. During MR scanning, RF energy is pulsed into the tissue to generate the MR images. Tissues involved would absorb some of the RF energy and will be heated up. Metallic devices can concentrate this RF energy, which might lead to excessive local heating, especially at the tip of those devices. This situation even gets worse when the device forms large loops. RF energy during MR scanning can also induce electrical current in wires and leads, which might possibly induce arrhythmias [22,23]. A time-varying magnetic field called gradient magnetic field is repeatedly and rapidly turned on and off to encode for various aspects of the image acquisition. This gradient magnetic field would induce electrical currents in electrically conductive devices and may directly excite peripheral nerves. More information about the basic principles, techniques and usages of MRI can be found elsewhere [15,24,25].

According to the international standard ISO 25539-2 "Cardiovascular Implants-Endovascular Devices—Part 2: Vascular Stents", MR safety and compatibility should be evaluated for vascular stents. Basically, safety items including magnetically induced displacement force, torque, and RF induced heating as well as compatibility item considering image artifact should be estimated [26]. Guidance for evaluating the above-mentioned items can be found in ASTM F2052 [27], ASTM F2213 [28], ASTM F2182 [29] and ASTM F2119 [30], respectively. The terminologies used for labeling vascular implants and their definitions are listed in Table 1. Test items and brief introduction of the test methods are summarized in Table 2.

1.4. Purpose of this study

The vast majority of currently used cardiovascular devices are either nonferromagnetic or weakly ferromagnetic [31]. Differing from currently used permanent DES or polymeric scaffolds, the nitrided iron

Table 1
Classification of implanted devices under MR environment and terminology used for labeling [30,31,44].

Classification	Definition	Label (Icons)
MR safe	An item that poses no known hazards in any MR environment. "MR safe" items are composed of materials that are electrically nonconductive, nonmetallic, and nonmagnetic, such as a plastic Petri dish.	MR
MR conditional	An item that has been demonstrated to pose no known hazards in a specified MR environment with specified conditions of use. Conditions that define the MR environment include static magnetic field strength, spatial magnetic gradient, dB/dt (time-varying magnetic fields), RF fields, and SAR (specific absorption rate). Additional conditions, including specific configurations of the item (eg, the routing of leads used for a neurostimulation system), may be required.	MR
MR unsafe	An item that is known to pose hazards in all MR environment, or to pose unacceptable risks to the patient, medical staff or other persons within the MR environment. "MR unsafe" items include magnetic items such as a pair of ferromagnetic scissors.	MR
MR compatible	A device shall be considered "MR compatible" if it is MR safe and the device, when used in the MR environment, has been demonstrated to neither significantly affect the quality of the diagnostic information nor have its operations affected by the MR system. The MR imaging conditions in which the device was tested should be specified in conjunction with the term "MR compatible," because a device that is safe under 1 set of conditions may not be found to be so under more extreme MR conditions.	NA

Table 2
Hazards to be tested of vascular stents considering their MR safety and compatibility (according to ASTM standards), but not limited to that.

| Category	Test item	Source of risk	Brief description of test method	Acceptance criterion/Reference point	Reference standard
MR safety	Magnetically induced displacement force	Gradient magnetic field	A medical device is suspended by a string in an MR system at a location near the entrance to the bore and on the axis of the bore. The angular deflection of the string from the vertical is measured.	If the device deflects less than 45°, then the magnetically induced deflection force is less than the force on the device due to gravity. It is assumed that any risk imposed by the magnetically induced force is no greater than any risk imposed by normal daily activity in the Earth's gravitational field.	ASTM F 2052-15
	Magnetically induced torque	Static main magnetic field	Five methods for measurement or assessment of magnetically induced torque are provided: the Suspension Method, the Low Friction Surface Method, the Torsional Spring Method, the Pulley Method, and the Calculation Based on Measured Displacement Force Method. In this work, the Torsional Spring Method was adopted. A torsion pendulum is used during the test. A device is placed on a holder suspended by a torsion spring. The apparatus is placed in the center of the magnetic resonance equipment magnet where the magnetic field is uniform. The torque is determined from the measurement of the deflection angle of the holder from its equilibrium position.	If the maximum magnetically induced torque is less than the product of the longest dimension of the medical device and its weight, then the magnetically induced torque is less than the worst-case torque on the device due to gravity. It is assumed that any risk imposed by the magnetically induced torque is no greater than any risk imposed by normal daily activity in the Earth's gravitational field.	ASTM F 2213-17
	RF induced heating	RF energy	The implant to be tested is placed in a phantom material that simulates the electrical and thermal properties of the human body. The implant is placed at a location with well characterized exposure conditions. The local SAR is assessed to characterize the exposure conditions at that location. Temperature probes are placed at locations where the induced implant heating is expected to be the greatest. The phantom is placed in an MR system. An RF field producing a sufficient whole-body averaged SAR of about 2W/kg averaged over the volume of the phantom is applied for approximately 15 min, or other time sufficient to characterize the temperature rise and the local SAR.	The results may be used as an input to a computational model for estimating temperature rise due to the presence of that implant in a patient. The combination of the test results and the computational model results may then be used to help assess the safety of a patient with the implant during an MR scan.	ASTM F 2182-11
MR compatibility	MR image artifacts	Magnetic interaction with implant device	Pairs of spin echo images are generated both with and without the implant in the field of view. Image artifacts are assessed by computing differences outside the region corresponding to the implant between reference and implant images. Once the worst-case conditions using the spin echo pulse sequence are ascertained, a pair of gradient echo image are acquired under the same conditions. This method only applies to passive implants that have been established to be MR safe or MR conditional.	Image artifacts under MR environment may lead to misinterpretation of image (image quality issues). This test method provides a quantified measurement of the image artifact produced under a standard set of scanning conditions.	ASTM F 2119-07
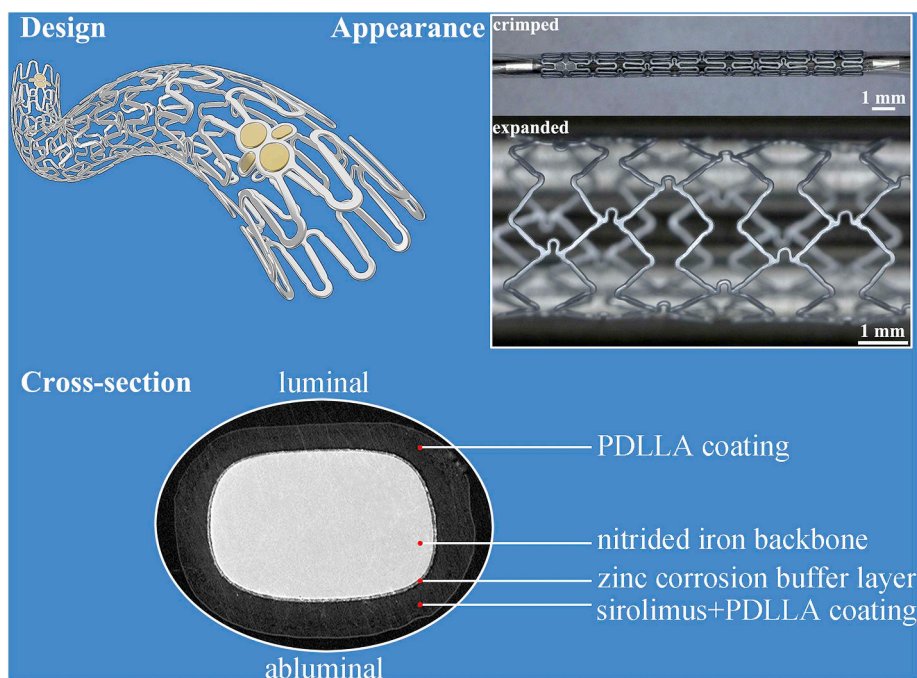
Fig. 1. General and cross-sectional illustrations of the IBS scaffold.

backbone of the IBS scaffold is a ferromagnetic material, and this poses possible dangers during MR examination. A comprehensive understanding of the MR safety and compatibility of this brand-new bioresorbable scaffold is needed. In the present research, MR safety and compatibility of the IBS scaffold was generally evaluated through well-designed *in-vitro*, *ex-vivo* and *in-vivo* experiments, specifically considering the ferromagnetic properties and biodegradation behaviors of this scaffold.

2. Material and methods

2.1. The investigational device

A typical IBS scaffold is basically composed of three components, i.e. the nitrided iron backbone with two sets of gold radiopaque markers at both ends, a pure zinc buffer layer, and a PDLLA-sirolimus coating, as displayed in Fig. 1. Gold markers are supplemented for enhancement of visibility under radiation. Sirolimus was concentrated in the PDLLA coating on the abluminal side of the strut. Scaffold design, processing, and other informative data including crossing profile, radial strength et al., can be found in our previous publications [11,32].

2.2. In-vitro characterization of the IBS scaffold under MR environment

As for the *in-vitro* evaluation, the investigational device, the IBS scaffold, was evaluated under commonly used MR conditions in clinic, considering the aspects of magnetically induced displacement force, magnetically induced torque, RF induced heating and MR image artifact. Experimental details were described below.

2.2.1. Test of magnetically induced displacement force

A MAGNETOM Trio magnetic resonance imaging system (A Tim System 3 T, Siemens Medical Solutions, Erlangen, Germany) equipped with a Numaris/4 (syngo MR B15) software was employed for the test. The maximum magnetic gradient was 40 mT/m with a scanning frequency of 200 Mt/m/ms. The test method and setup were in accordance with the recommendations in ASTM F2052-15 [27], as shown in Fig. 2 (a). In brief, the test device was suspended by a string near the entrance of the MRI bore. The weight of the string could be negligible, definitely

less than 1% of the device weight. The angle of deflection was recorded through a protractor mounted on the fixture. Three parallel measurements were made. Calculate the magnetically induced displacement force through the deflection angle α by following the equation: $F_m = mg \cdot \tan\alpha$, where m is the mass of the device, and g is the acceleration of gravity.

As we mentioned before, backbone material of the IBS scaffold is nitirded iron and it is ferromagnetic. Deflection angle α of the IBS scaffold under MR environment is approximate to 90°, which means the value of tanα is quite large. Any minor fluctuation of the measured α makes a big difference on the calculated F_m value, which makes the measurement hard to perform. In order to solve this problem and to get a reliable result, a nonmagnetic plasticine was stuck to the scaffold centroid to add the mass, in this way, to lower the α value to ~45°. By doing so, an accurate and repeatable measurement could be made.

2.2.2. Test of magnetically induced torque

The earlier mentioned MAGNETOM Trio magnetic resonance imaging system was employed in the test of magnetically induced torque. The largest and heaviest specification of IBS-40038 was tested since magnetically induced torque is in positive correlation with sample mass/volume. For qualitative analysis, the scaffold was placed on a plastic board with smooth surface under the MR environment. Change the axial direction of the scaffold to form different intersection angles with the direction of the main magnetic field. The speed that the device returned to the equilibrium position was record and evaluated. For quantitative analysis, the test method and setup were in accordance with the recommendations in ASTM F 2213-17 [28], as depicted in Fig. 2 (b). Briefly, the IBS scaffold was mounted on the holding platform after mass weighing. The apparatus was placed in the center of the MR scanner, where the magnetic field is uniform. The frame holding the spring and holder assembly was rotated, and the torque as a function of angle of the implant was determined. The test angle range was 0–360°, with a rotating step size of 10°.

2.2.3. Test of RF induced heating

Test setup and test procedure of RF induced heating was referred to the recommendations in ASTM F 2182-11a [29]. A phantom material was utilized to simulate the electrical and thermal properties of the
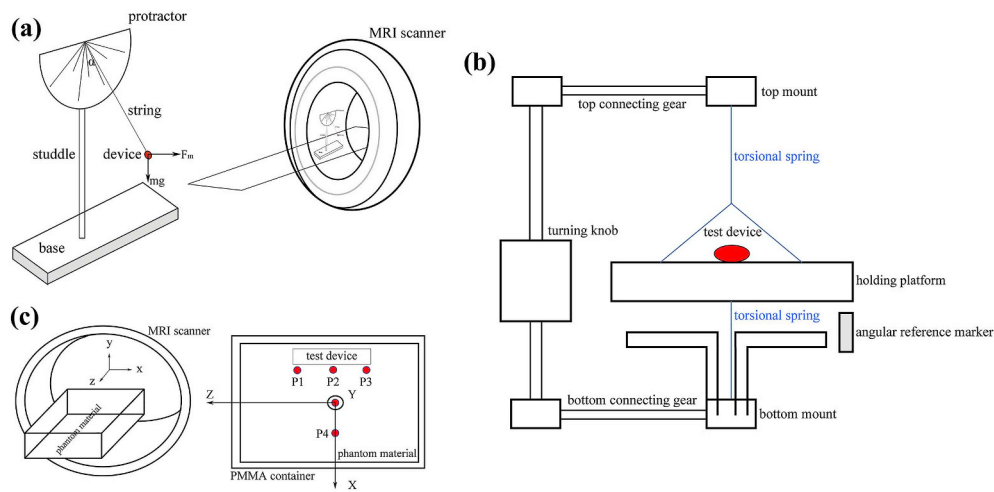
Fig. 2. (a) Schematic diagram of the test fixture mounted on the MR scanner during magnetically induced displacement force test, (b) torsion spring apparatus used for magnetically induced torque test, (c) an apparatus for testing of RF induced heating near the IBS scaffold, and temperature probes distribution in the measurement of RF induced heating.

Table 3
Scanning parameters during the RF induced heating test and MR imaging parameters for artifacts testing.

RF induced heating test		MRI artifacts test		
Scanning parameter	Setting	Scanning parameter	Setting value	
Slices	20	Pulse sequence type	Spin-Echo	Gradient-Echo
RF pulse type	Fast	TR (repetition time)	500 ms	500 ms
Dist factor	30%	TE (echo time)	20 ms	15 ms
Orientation	Coronal	Collection times	1	1.5
Phase enc dir	RL	Matrix size	180×180	180×180
Field of view (FOV)	500 mm	Field of view	18 cm	18 cm
Bandwidth	337 Hz	Bandwidth	300 Hz	217 Hz
Slice thickness	4 mm	Slice thickness	2 mm	2 mm
TR (repetition time)	4470 ms	Flip angle	70°	30°
TE (echo time)	62 ms	NA		
Averages	10			
Flip angle	115°			
Time duration	15 min			

human body. This material was obtained by mixing 1.32 g/L NaCl with 10 g/L polyacrylic acid (PAA) to get a suitable conductivity (0.47 ± 10% S/m), a proper relative electric permittivity (80 ± 20 at the appropriate test frequency 64 MHz or 128 MHz), suitable thermal parameters (a diffusivity of about 1.3×10^{-7} m²/s and a heat capacity of 4150 J/kg·°C), and a viscosity sufficient to prevent convective heat transport. The phantom material was held in a polymethyl methacrylate (PMMA) container, which was electrical insulating and non-magnetic. The largest IBS scaffold (40038) was placed in the phantom material with well characterized exposure condition. Temperature probes were placed at locations where the induced heating is expected to be the greatest. A sketch of the test apparatus and temperature probes distribution are displayed in Fig. 2 (c). The phantom was placed in the MR system. The heating measurements were made twice, once with the implant and then repeated at the same location without the implant. The local SAR and the local additional temperature rise with the implant could be estimated through these two measurements. Scanning parameters adopted during the RF induced heating test are listed in Table 3.

2.2.4. Test of MR image artifacts

MR image artifacts tests were performed according to ASTM F 2119-07(2013) [30]. Artifacts of the IBS scaffold is related to the scaffold mass and imaging parameters. So, the heaviest specification IBS-40038 was chosen as the experimental device to represent the worst case. Briefly, the test device was immersed in 1.5 g/L CuSO₄ solution, a solution to keep TR (repetition time) at a reasonable level. Position of the device was fixed to ensure any movement of the device was avoided. To

achieve an adequate field homogeneity, at least 4 cm of clearance between the device and each side of the container holding the solution and the implant should be reserved. A nylon rod with a diameter of 0.5 inch was utilized as a reference material in each image acquired. Then, a circle appeared in the image could serve as a reference object. The maximum distance from the edge of the device to the fringe of the resulting image artifact found in the entire set of images was defined as the artifact width. Detailed MR imaging parameters during artifacts testing were listed in Table 3.

2.3. Ex-vivo evaluation of the scaffold-artery system under simulated force-bearing conditions

Due to the inherent ferromagnetism of iron, the force that an IBS scaffold would bear under MR environment might cause possible scaffold displacement and corresponding artery injury. Potential failure modes or possible injuries caused by the IBS scaffold under MR environment include scaffold falling-off or movement (deviation from the designated position), puncture of the intima, or puncture of the artery wall. *Ex-vivo* experiments were employed to evaluate the risks upon those aspects under the worst load-bearing conditions. The worst load-bearing conditions were determined based on the *in-vitro* testing results.

External force was applied on a scaffold, which was dilated in an *ex-vivo* rabbit abdominal aorta, through two approaches to evaluate the risks of scaffold displacement and possible vascular injuries. In the first case, an IBS-40038 scaffold was dilated in a dissected rabbit artery with normal diameter. Then, a force was vertically applied on the dilated scaffold through hanging a 5 g (equivalent to 0.049 N, to simulate the

worst-case magnetically induced displacement force) counterweight for 15 min, as shown in Fig. 5 (a). Any displacement of the scaffold referred to the artery and any injuries on the artery were recorded. In the second case, an artery segment was cut open and flattened on a glass plate. A shorter specification IBS-30008 (nominal pressure (NP) dilated) was vertically placed on the flattened artery, and then a vertical force was applied on the upper end of the scaffold, as shown in Fig. 5 (b). Increase the force gradually (1 mm/min) until the scaffold losing its stability or collapsing. Any puncture on the artery after removal of the scaffold was closely observed both under naked eyes and under an optical microscope (VHX-700F, KEYENCE).

2.4. In-vivo evaluation of the IBS scaffold under MR environment

2.4.1. Animal model and surgical procedures

New Zealand white rabbits were chosen as the experimental animal model for *in-vivo* MR evaluation after IBS implantation. Scaffolds were implanted in the abdominal aorta. Briefly, the iliac artery was surgically exposed and a 5F guide catheter was intruded over a 0.014 inch guidewire. The IBS scaffold was placed at the predetermined position and dilated under angiography. Animals were fed with a standard diet without cholesterol or lipid supplementation with free access to clean drinking water throughout the experiment. The surgical procedures and post-operative care protocols were fulfilled the requirements of the the Ethics Committee of the Shenzhen Advanced Medical Services Co., Ltd.

2.4.2. Evaluation of possible scaffold displacement and vessel injury under MR environment

Before scaffold deployment, diameter of the abdominal aorta was measured through digital subtraction angiography (DSA). Two IBS-30015 scaffolds were implanted in the abdominal aorta one behind the other. The proximal one was dilated at a scaffold/artery diameter ratio of approximating to 1.0, and the distal one was dilated at a scaffold/artery diameter ratio of 1.1–1.2. The experimental animal was scanned under a typical 3T MR environment immediately after the two scaffolds were successfully implanted. After the MR scanning, DSA was once again performed with the same parameters as those before scaffold implantation. Positions of those two scaffolds before and after MR scanning were recorded, respectively. Any movement of the scaffold from the designated position should be noted. Any tearing or puncture of the scaffolded artery was clearly inspected under an optical microscope after dissection of the abdominal aorta.

2.4.3. In-vivo MR image artifacts

Animals received IBS implantation were examined under a MR scanner (*in-vivo* scanning) at different periods after surgery (0 d, 6 m and 13 m). At predetermined time intervals, animals were euthanized. Afterwards, the scaffolded artery sections were retrieved, and also scanned under the MR scanner (explant scanning). The artifact width was measured. Retrieved scaffolds were examined under a micro-CT scanner (Skyscan1172, Bruker). Then, the retrieved scaffolds were immersed in ethyl acetate to remove the remaining polylactic acid coating. The scaffolds were transferred into a tartaric acid solution to remove the corrosion products. Afterwards, they were cleaned in absolute ethanol and dried in the open air. The weight loss of the remaining nitrided iron backbone was measured.

2.5. Statistical analysis

Quantitative results are expressed as mean $\pm$ standard deviation. Statistical differences were analyzed by using the analysis of variance (ANOVA), and $p < 0.05$ was considered statistically significant.

3. Results

3.1. In-vitro

3.1.1. Magnetically induced displacement force

Magnetically induced displacement forces of various scaffolds with different nominal diameters, lengths and strut thicknesses (diameter: 3.0 and 4.0 mm, length: 8, 15 and 38 mm, strut thickness: 53 (final design of IBS scaffold Φ3.0 mm), 60 (final design of IBS scaffold Φ4.0 mm) and 70 μm (design during R&D)) were measured in the MR scanner at the site where the maximum gradient magnetic field appears. Test results are displayed in Fig. 3 (a), and more detailed data are listed in Table 4. The magnetically induced displacement force is in directly proportional to the scaffold mass, and they are in a linear law, as depicted in Fig. 3 (a). The largest/heaviest scaffold during magnetically induced displacement force test was the 40038 (70 μm, during R&D) one, and it suffered the largest force with a value of 0.03277 N. The measured force is ca. 90 times higher than the scaffold gravity, as shown in Table 4. For the final-designed IBS scaffolds, the magnetically induced displacement force of IBS-40038 (60 μm) was 0.02599 N. Magnetically induced displacement force decreases along with the scaffold degradation, as the average force (IBS-30008, 53 μm) significantly decreases from $(33.40 \pm 0.12) \times 10^{-4}$ N to $(5.30 \pm 4.06) \times 10^{-4}$ N (with a reduction of 6 times) after 1 years in rabbit abdominal aorta.

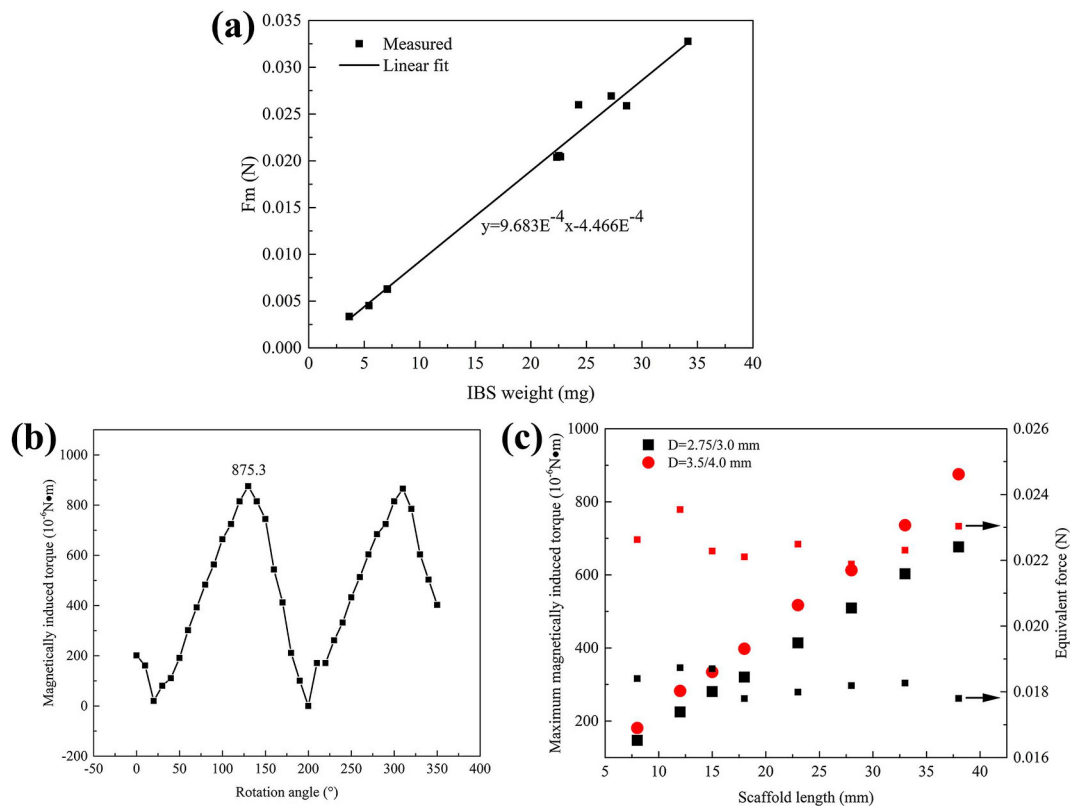#### 3.1.2. Magnetically induced torque

For qualitative assessment, the device (IBS-40038) was placed on a plastic board with smooth surface under the MR environment. The IBS scaffold suffered an extremely strong torque compared to its gravity, as the device axis turned and aligned into the magnetic field direction extremely fast and mighty, as shown in Table 5. Fig. 3 (b) displays the quantitative results showing the variation of magnetically induced torque during a full 360° rotation. From the aspect of electromagnetism, it is well-known that the maximum and minimum torques appear at the spatial positions when the scaffold is perpendicular to and parallel to the magnetic field direction, respectively. Two peaks accompanied with two valleys were detected on the curve, implying two orientations being perpendicular to and parallel to the magnetic field direction, respectively. The minimum value came close to 0 N•m, and the maximum value was 8.753×10^{-4} N•m, which was far higher than (> two orders of magnitude) the gravitational torque. The worst-case torque induced by the gravity of the scaffold itself is only 8.193×10^{-6} N•m. The maximum magnetic torque 8.753×10^{-4} N•m is equivalent to apply a force (equivalent force) of 0.023 N perpendicularly to the end of the scaffold. Since the magnetically induced torque is proportional to the volume/mass of the scaffold, the maximum magnetic torques and corresponding equivalent forces of all the IBS specifications could be extrapolated, which is displayed in Fig. 3 (c) and in Table 6. For a same platform (Φ = 2.75/3.0 mm or Φ = 3.5/4.0 mm), the equivalent forces of different scaffold lengths were similar, as the torque is determined by both scaffold mass and length.

3.1.3. RF induced heating

Test results of RF induced heating are displayed in Table 7 below. For the investigational device, the maximum RF induced heating appeared at the end of the scaffold. As for slim/elongated device (long and thin), the maximum temperature rise generally appears at the endpoint of the device, and implant heating may also be maximal at sharp corners or edges [29]. Under a whole body (phantom) averaged SAR condition of 2.0 W/kg, the estimated maximum temperature rise around the largest IBS specification (40038) was only 1.27 °C.

3.1.4. MR image artifacts

The largest IBS specification (40038) for coronary arteries was evaluated for artifacts under Spin-Echo (SE) and Gradient-Echo (GRE)

Fig. 3. (a) Measured displacement forces of various IBS scaffolds and corresponding linear fitting result, (b) magnetically induced torque of IBS-40038 at various directions in the MR scanner under 3 T, (c) the maximum magnetically induced torques and corresponding equivalent forces of all the IBS specifications for coronary arteries.

pulse sequences, respectively. Typical MR images and how the image artifact width was measured are shown in Fig. 4. How the scaffold was placed in the MR scanner (parallel or perpendicular to the main magnetic field) did not make too much differences in artifact morphologies.

So, only the case in which the scaffold was placed perpendicular to the main magnetic field was displayed. The artifact widths in the directions of transverse and sagittal planes were measured, and corresponding results are listed in Table 8. Image artifacts under different scanning

Table 4
Sample description and test parameters during magnetically induced displacement force test.

Sample category	Scaffold specification[a]	Strut (nitrided iron backbone) thickness (μm)	Sample size	Scaffold weight (mg)	Scaffold + plasticine weight (g)	Deflection angle α (°)	Scaffold gravity (10^{-5} N)	Magnetically induced displacement force F_m (N)	F_m/ Scaffold gravity
Original scaffold	30008	53	3	3.6493	0.3080	48.0	3.57631	0.00335	93.67
				3.6517	0.3130	47.5	3.57867	0.00335	93.61
				3.6515	0.3110	47.5	3.57847	0.00333	93.06
	30015	53	3	7.0980	0.6660	44.0	6.95604	0.00630	90.57
				7.0850	0.6360	45.1	6.94330	0.00626	90.16
				7.0780	0.6460	44.8	6.93644	0.00629	90.68
	40038	53[c]	3	22.3460	2.1610	43.9	21.89910	0.02038	93.06
				22.6740	2.1430	44.2	22.22050	0.02042	91.90
				22.5210	2.1870	43.8	22.07060	0.02055	93.11
	40038	60	1	24.3000	5.2059	27.0	23.81400	0.02599	109.13
	30008	70[c]	1	5.4370	0.5290	41.0	5.32826	0.00451	84.64
	30038	70[c]	1	28.6234	2.6863	44.5	28.05090	0.02587	92.23
	40038	70[c]	1	34.1469	3.1182	47.0	33.46400	0.03277	97.93
Retrieved implant with tissue after 1 year in rabbit abdominal aorta	30008	53	3	3.4530	0.0445	66.0	3.38394	0.00098[b]	28.96
				3.5420	0.0704	31.0	3.47116	0.00042[b]	12.10
				3.3240	0.0597	17.8	3.25752	0.00019[b]	5.83

[a] For a given scaffold specification, such as 30015, the first three digits mean the diameter of this scaffold under nominal pressure (NP = 8 atm) is 3.00 mm, and the last two digits mean the scaffold length is 15 mm.

[b] F_m (N) of IBS-30008 (53 μm) after 1 years in rabbit abdominal aorta is significantly different from that of the original scaffold itself (p < 0.01).

[c] The 70 μm-thickness scaffolds and 40038 (53 μm) were samples during IBS R&D process, not the final design, and they were only used for magnetically induced displacement force analysis in this study. Final-designed IBS samples were used in the remaining tests in this study. Final strut (nitrided iron backbone) thickness design of IBS scaffold was 53 μm for Φ3.0 mm and 60 μm for Φ4.0 mm.

Table 5
Qualitative assessment of magnetically induced torque of the IBS scaffold.

Angle between the scaffold axis and the magnetic field direction (°)	0	45	90	135	180	225	270	315
Testing result (classification)	4	4	4	4	4	4	4	4
Classification and definition of magnetically induced torque during qualitative assessment	0 without torque, no movement of the device. 1 minor torque, minor movement of the device toward the magnetic field direction, but still not aligning to. 2 medium torque, the device slowly turns and aligns to the magnetic field direction. 3 strong torque, the device axis turns and aligns to the magnetic field direction pithily. 4 extremely strong torque, the device axis turns and aligns to the magnetic field direction extremely fast and mighty.

sequences (SE/GRE) in different directions appeared in totally different morphologies. Under SE sequence, the images were surrounded by highlighted areas with obvious trailing traces. Meanwhile, image artifacts under GRE sequence were relatively regular. The maximum overall-artifact width was found to be 119.5 mm at the sagittal direction under SE sequence type when the scaffold was placed perpendicular to the main magnetic field.

3.2. Ex-vivo

The maximum force that an IBS scaffold might bear under the commonly clinical MR environment was determined in the *in-vitro* testing section, and it was referenced in the *ex-vivo* experiment. Is there any possibility that such a force applied on the scaffold might cause any movement of the scaffold or puncture through the artery wall? In order to figure this out, the *ex-vivo* bench testing was carried out. The maximum magnetically induced displacement force was measured to be 0.02599 N (IBS-40038). The maximum magnetically induced torque was 8.753×10^{-4} N•m, and it corresponded to a 0.023 N equivalent force. Then, a shear stress of 0.049 N (much higher than the magnetically induced displacement force) and a maximum normal stress of 0.35 N (ca. 10-fold amplification) were applied in the *ex-vivo* experiments to assess the risks of scaffold displacement and corresponding vessel injury (puncture) under MR environment.

In case 1 situation displayed in Fig. 5 (a), there was no observable displacement of the scaffold relative to the artery, as the scaffold was well attached in the *ex-vivo* artery. After removal of the additional counterweight, no tearing or puncture of the intima was found. The external shearing stress can be balanced by the frictional force between the scaffold and the artery if the scaffold was dilated with a scaffold/artery diameter ratio of 1.1:1~1.2:1. In case 2 situation displayed in Fig. 5 (b), the external normal force perpendicular to the vessel wall was utilized to evaluate the possibility of any puncture induced by the
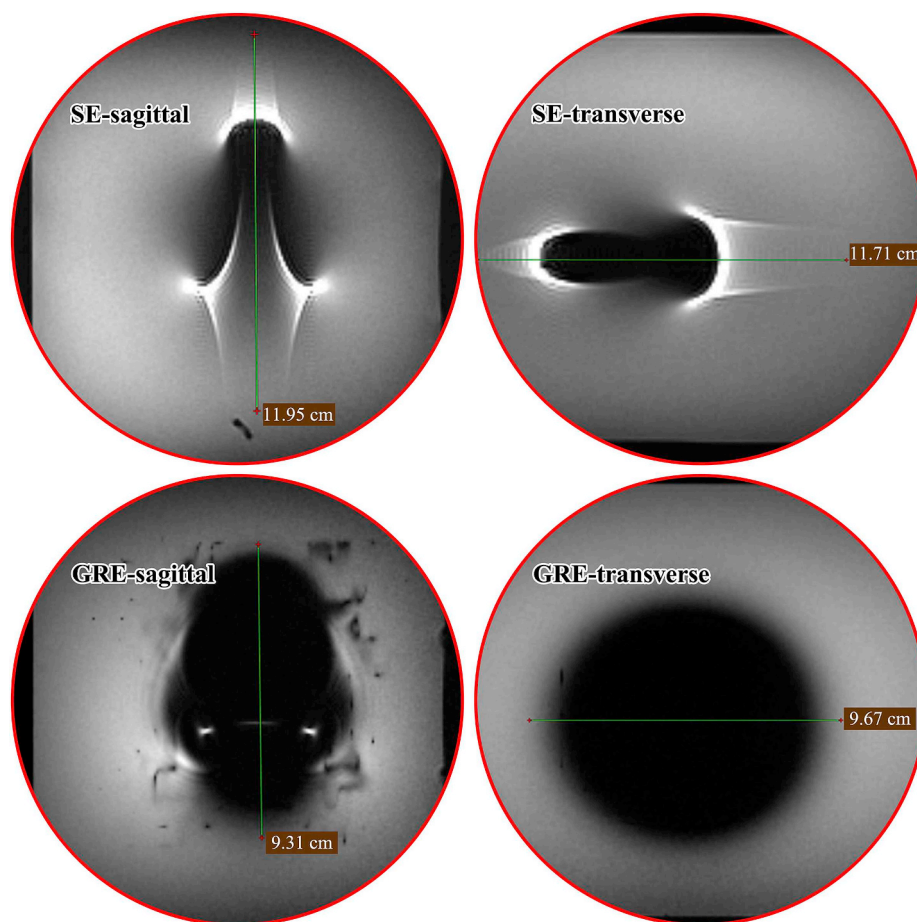
Table 6
The maximum magnetically induced torques and corresponding equivalent forces of all the IBS specifications for coronary arteries. Scaffolds with nominal diameters of Φ2.75 mm and Φ3.0 mm series share a same platform (same pattern), and Φ3.5 mm and Φ4.0 mm specifications share another platform.

Diameter (mm)	Length (mm)															
	Magnetically induced torque (10^{-6} N•m)								Equivalent force (N)							
	8	12	15	18	23	28	33	38	8	12	15	18	23	28	33	38
2.75 3.0	147.21	224.79	280.49	320.28	413.78	509.27	602.76	676.37	0.018	0.019	0.019	0.018	0.018	0.018	0.018	0.018
3.5 4.0	181.03	282.48	334.21	397.86	517.22	612.71	736.05	875.30	0.023	0.024	0.022	0.022	0.022	0.022	0.022	0.023

Table 7
Test items and corresponding results of RF induced heating of IBS-40038.

Items	Test results			
Averaged SAR of phantom				
Room temperature (°C)	19.00			
Scanning duration (s)	900			
Initial temperature of the phantom material (°C)	18.69			
Final temperature of the phantom material (°C)	19.24			
Calculated SAR value (W/kg)	2.53			
Temperature rise with the device				
Initial temperature at the beginning of the scanning T_i (with device) (°C)	P1 (T_i) = 17.14	P2 (T_i) = 17.15	P3 (T_i) = 17.15	P4 (T_i) = 16.82
Final temperature of the scanning T_f (with device) (°C)	P1 (T_f) = 18.75	P2 (T_f) = 17.93	P3 (T_f) = 18.50	P4 (T_f) = 17.33
Temperature rise $\Delta T = T_f$-T_i (with device) (°C)	$\Delta T1$ = 1.61	$\Delta T2$ = 0.78	$\Delta T3$ = 1.35	$\Delta T4$ = 0.51
SAR value with device (W/kg)	7.42	3.60	6.23	2.35
Maximum temperature rise ΔT_{max} (with device) (°C)	1.61			
Temperature rise without the device (background temperature rise)				
Initial temperature at the beginning of the scanning T_i (without device) (°C)	P1 (T_i) = 19.58	P2 (T_i) = 17.88	P3 (T_i) = 18.39	P4 (T_i) = 18.62
Final temperature of the scanning T_f (without device) (°C)	P1 (T_f) = 20.08	P2 (T_f) = 18.10	P3 (T_f) = 18.80	P4 (T_f) = 18.99
Temperature rise $\Delta T = T_f$-T_i (without device) (°C)	$\Delta T1$ = 0.5	$\Delta T2$ = 0.22	$\Delta T3$ = 0.41	$\Delta T4$ = 0.37
SAR value without device (W/kg)	2.31	1.01	1.89	1.71
Temperature rise induced by device ΔT_{device} (°C)	1.11	0.56	0.94	0.14
Maximum temperature rise ΔT_{max} at the condition of the whole body averaged specific absorption rate (WSAR) = 2.0 W/kg (with device)	1.27			

Fig. 4. Typical MR images showing how the image artifact width was measured in the directions of transverse and sagittal planes (the scaffold was placed perpendicular to the main magnetic field).

scaffold edges. The scaffold lost its stability as the force increased from 0.1 N to 0.35 N. Even under this extreme condition, no tearing or puncture was found on the artery segment.

3.3. In-vivo

3.3.1. Scaffold displacement related to scaffold/artery diameter dilation ratio

Fig. 6 displays the scaffold movement caused by MR scanning immediately after IBS implantation. Position of the IBS scaffold could be identified by the distal gold marker under DSA. Two scaffolds with different scaffold/artery diameter ratios during dilation exhibited totally different results. The scaffold with a scaffold/artery diameter ratio of 1.0 was forced to deviated from its originally designated position. A 2 mm displacement could be measured after MR scanning. For the one with a scaffold/artery diameter ratio of 1.1–1.2, no movement was observed. There were no signs of tearing or rupture of the intima under both angiography examination and under anatomical observation.

3.3.2. MR image artifacts in vivo

Fig. 7 displays the MR image artifacts in animals carried with IBS scaffolds (in-vivo scanning), and also in retrieved scaffold-artery samples (explant scanning), along with the explant micro-CT examination. Three IBS-30008 scaffolds were implanted one after another (2–3 cm between each other) in the rabbit abdominal aorta. The scaffold kept intact at 6 months, while it was partially corroded as the remaining strut (black entity) was surrounded by light-gray corrosion products. The nitrided iron backbone was severely corroded after 13 months, and only limited fragmentary struts could be found under micro-CT

examination. MR image artifacts at the ends of the three IBS scaffolds in vivo were overlapped till 6-month post-implantation. The extent of the artifacts gradually decreased along with implantation time. There was no overlapping in the image artifacts of the three individual IBS scaffolds at 13 months. The artifact area and the maximum artifact width gradually decreased along with implantation time, i.e. along with scaffold degradation, as depicted in both in-vivo scanning and explant scanning, which means distortion of the MR images was lowered as IBS degradation proceeding. Even though the nitrided iron backbone was 83.6 ± 11.1% corroded at 13 months, a small area of MR image artifacts derived from the remaining struts and corrosion products still existed at the position where the original scaffold used to be, as marked by red arrows.

4. Discussion

4.1. MR safety of the IBS scaffold

4.1.1. MR safety immediately after IBS implantation

According to the test methods recommended in ASTM standards, temperature rise around the IBS scaffold was 1.27 °C, which was within the normal fluctuation range of human body temperature [33]. Considering the cooling effect of blood perfusion, the actual temperature rise should be even lower. So, RF induced heating of the IBS scaffold is not a concern during MR examination.

There is no specific criterion which clearly specifies the values of the magnetically induced displacement force and magnetically induced torque, below which the device can be categorized as MR safe. Commonly, for a device characterized as MR safe, magnetically induced
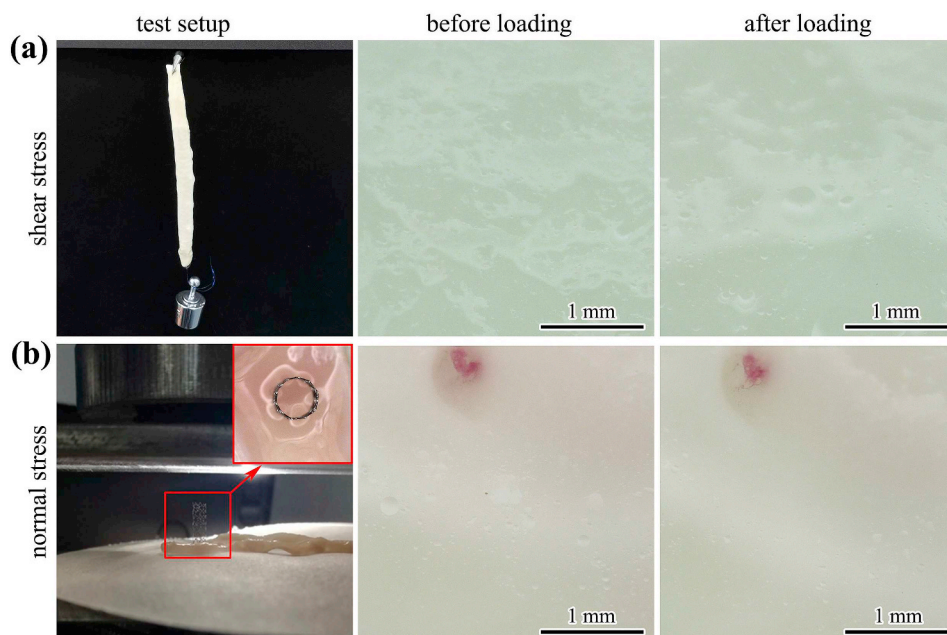
Fig. 5. *Ex-vivo* evaluation of the scaffold-artery system under simulated force-bearing conditions, schematic test setups and corresponding artery inspection: (a) a shear stress was applied on the scaffold-artery system to see whether any relative displacement or artery injury would happen, (b) a normal stress was applied on the scaffold-artery system to see whether any puncture would happen on the dissected vessel.

Table 8
Test results of MR image artifacts under both SE and GRE pulse sequence types.

Sample position (scaffold axis to the main magnetic field)	Pulse sequence type	Test orientation	Overall artifact width (mm)	Unilateral artifact width (mm)[d]
Parallel	Spin-Echo (SE)	sagittal	107.1	34.6
		transverse	90.4	43.2
	Gradient-Echo (GRE)	sagittal	114.8	38.4
		transverse	77.8	36.9
Perpendicular	Spin-Echo (SE)	sagittal	119.5	57.8
		transverse	117.1	39.6
	Gradient-Echo (GRE)	sagittal	93.1	44.6
		transverse	96.7	29.4

[d] Unilateral artifact width means the maximum distance (mm) from the edge of the implant to the fringe of the resulting image artifact.

displacement force and magnetically induced torque of this device are lower than its gravity and gravitational torque, respectively. However, this does not mean a device is definitely MR unsafe if magnetically induced displacement force and magnetically induced torque are higher than the corresponding device gravity and gravitational torque. The judgement should be concluded based on a scientifically based rationale rather than only based on the test data [29].

The magnetically induced displacement force and torque are far higher than the IBS gravity and gravitational torque, respectively.

However, we still cannot make a conclusion on whether is it safe to perform MR examination after IBS implantation based on the above data. Potential failure modes or possible injuries caused by the IBS scaffold under MR environment include scaffold movement (deviation from the designated position), puncture of the intima, and puncture of the artery wall. Supplementary *ex-vivo* and *in-vivo* experiments were basically designed considering those aspects. The worst load-bearing conditions were explored during the *in-vitro* test. These extreme conditions were inspected via *ex-vivo* and *in-vivo* tests. Tearing or puncture
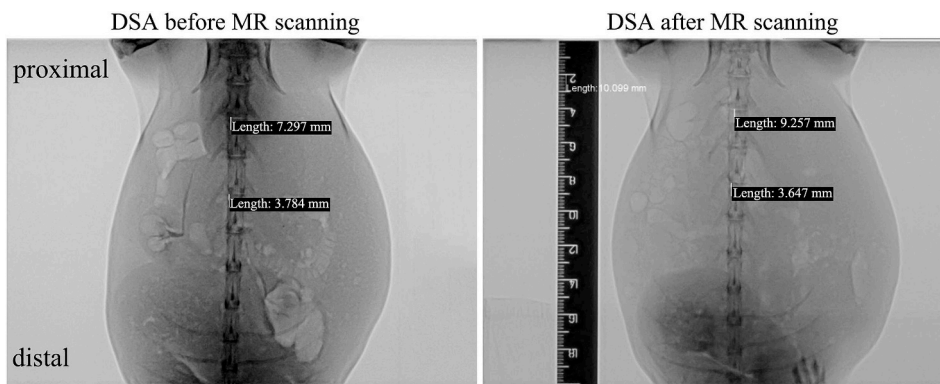
Fig. 6. Scaffold movement caused by MR scanning immediately after IBS implantation at different scaffold/artery diameter ratios (position of the IBS scaffold could be identified by the distal gold marker under DSA).
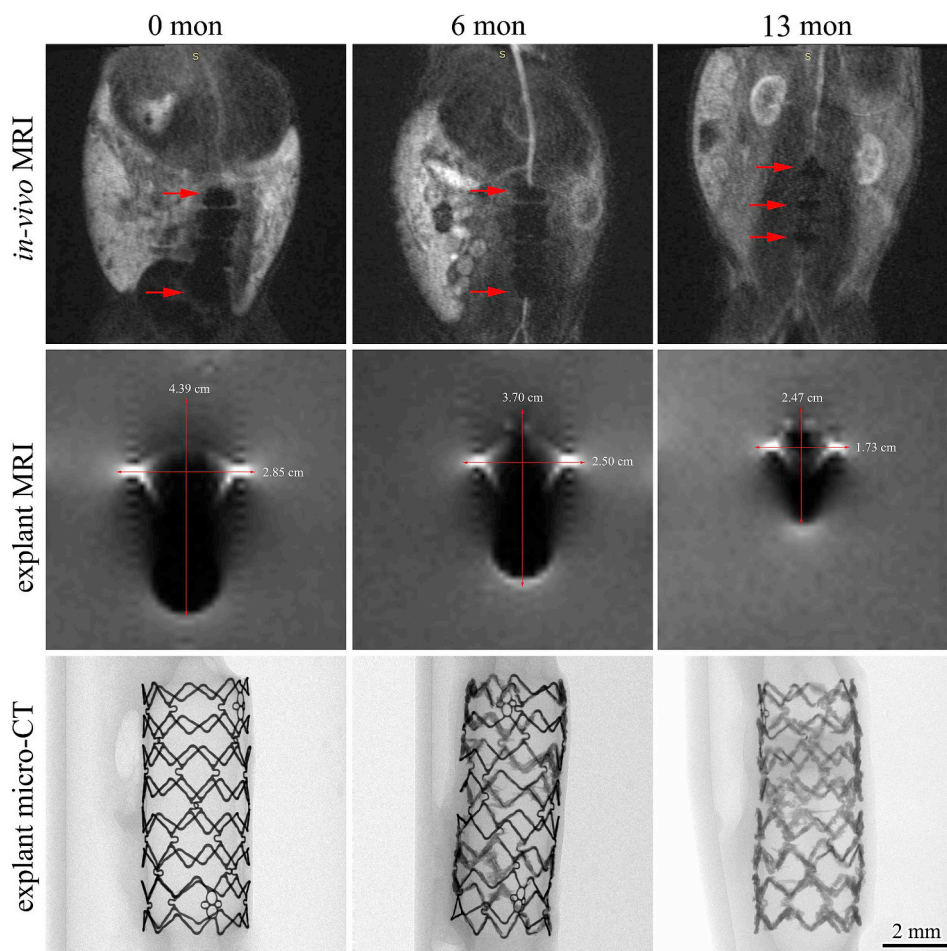
Fig. 7. *In-vivo* and explant (embedded in agar) MR images showing MR artifacts at different implantation periods and corresponding explant micro-CT analysis.

of intima or arterial wall was not observed in simulated load-bearing conditions of *ex-vivo* study and also in *in-vivo* experiments under MR environment. Possible risks of scaffold displacement in MR environment should be separately discussed, considering the anchor effect of vessel wall to the scaffold. Close attention should be paid if the scaffold was insufficient dilated or incomplete apposition occurred. Under this circumstance, the scaffold might be forced to leave the original position. According to our *ex-vivo* and *in-vivo* experiments, there is little chance for scaffold shift under MR scanning if a proper scaffold/artery diameter ratio (1.1:1–1.2:1) was chosen, and if the scaffold was well embedded in the artery wall. However, the difference between *ex-vivo/in-vivo* simulations and the actual clinical situations could not be ignored. *Ex-vivo* and *in-vivo* simulations were highly simplified. They may not fully represent the actual clinical situations, as specific patient might have complex artery disease, such as highly distorted artery profile, severe calcification, etc.

4.1.2. Time-relevant properties of the IBS scaffold under MR environment

Component elements of the IBS scaffold include metallic elements consisting of iron (Fe, backbone), zinc (Zn, buffer layer) and gold (Au, radiopaque marker), and nonmetallic elements consisting of carbon (C, PDLLA and sirolimus), hydrogen (H, PDLLA and sirolimus), oxygen (O, PDLLA and sirolimus) and nitrogen (N, sirolimus and backbone nitrided iron). Among all the component elements, only Fe belongs to the ferromagnetic category [34]. Possible safety issues of this scaffold under MR environment mainly derive from the backbone nitrided iron. Other constituent substances on the IBS scaffold including Zn, Au, PDLLA and sirolimus are all nonmagnetic, and they will not pose additional risks under MR environment.

Except for the tiny Au markers, other components on the IBS scaffold can be gradually degraded or corroded, and finally be metabolized or resorbed without any residuals. Possible risks caused by the corrosion/degradation products during IBS degradation were generally discussed here. The degradation product of PDLLA is micromolecular polylactic acid with low molecular weight, and the intermediate micromolecules can be finally metabolized into CO_2 and H_2O [35]. All the by-products during PDLLA degradation are nonmagnetic, and no extra risks under MR environment will be posed. The antiproliferative drug sirolimus itself and its hydrolysis products are nonmagnetic, so they will not bring new safety risks during MR examination. Possible corrosion products of the Zn corrosion buffer layer (~600 nm) are $Zn_3(PO_4)_2$, $ZnCO_3$, ZnO and $Zn(OH)_2$ [36]. No safety issues should be concerned with Zn corrosion under MR environment as both the pure Zn itself and its corrosion products are nonmagnetic. Ahead of the onset of backbone iron corrosion, magnetically induced displacement force, torque and RF induced heating of the IBS scaffold under MR environment should be nearly unchanged. The only doubt lies in the backbone iron corrosion as ferromagnetic corrosion products could be formed along with Fe corrosion. According to our previous *in-vivo* study of iron scaffold, possible corrosion products of Fe in animal artery were characterized to be $Fe(OH)_3$, γ-FeOOH, Fe_3O_4, α-Fe_2O_3 and $Fe_3(PO_4)_2$, among which only Fe_3O_4 is characterized to be ferromagnetic [13]. When Fe turns into Fe_3O_4, the magnetic susceptibility decreases. In addition, not all the Fe could transform into Fe_3O_4. Generally, the magnetically induced displacement force, magnetically induced torque, RF induced heating and MR image artifacts are gradually decreased as the IBS scaffold degradation proceeding.

Another issue that bioresorbable scaffolds may face with is that strut
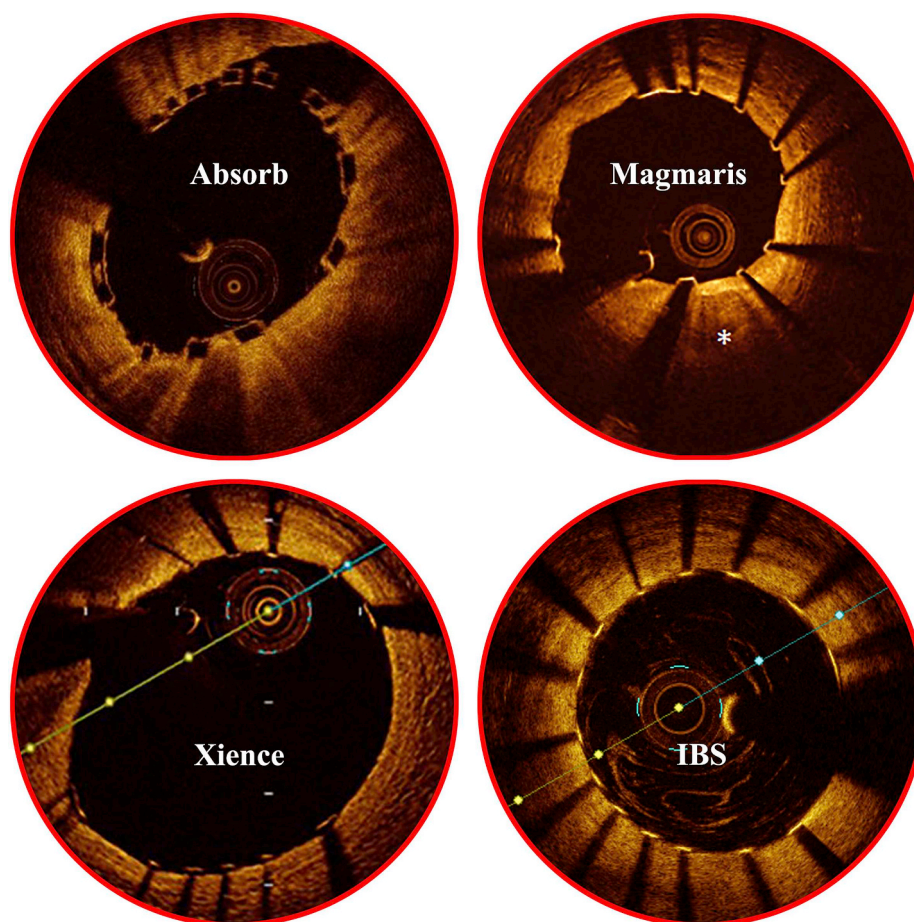
Fig. 8. Optical coherence tomography (OCT) images of one prevailing DES Xience (Abbott), one drug-eluting bioresorbable magnesium-based scaffold Magmaris (Biotronik), and one drug-eluting bioresorbable polymeric scaffold Absorb (Abbott) compared to an IBS scaffold (Biotyx) immediately after implantation [38–40].

fracture would happen during scaffold degradation [37]. If scaffold strut punctures through the intima and intrudes into the lumen without endothelialization, thrombosis might happen [6]. The ultrathin strut and abluminal drug loading design of IBS makes it easy to be embedded into the artery wall and favors for endothelialization. Fig. 8 displays the optical coherence tomography (OCT) images of one prevailing DES (Xience, Abbott) [38], one drug-eluting bioresorbable magnesium-based scaffold (Magmaris, Biotronik) [39], and one drug-eluting bioresorbable polymeric scaffold (Absorb, Abbott) [40] compared to an IBS scaffold (Biotyx) immediately after implantation. The scaffold is well apposed and the strut is well embedded in the artery wall, without too much protruding of the strut into the bloodstream. In a previous study, the IBS scaffold was characterized to be completely endothelialized within 28 days in a porcine model [9]. After full endothelialization, the movement of scaffold under MR environment should be basically eliminated. The onset of backbone iron corrosion is proposed to be 3–6 months after implantation. At this time point, endothelialization has totally completed. All of the scaffold struts will be surrounded and immobilized by tissues. Degradation of IBS was characterized to be generally uniform [11]. There is little possibility that sharp tips or incisive fracture surfaces would be generated after strut fracture caused by degradation. Besides, the residually uncorroded iron struts are surrounded by the solid corrosion products of iron [13]. The solid corrosion product can act as a buffering layer, relaxing the possible stress concentration at the fracture sites and reducing the irritation to the intima/vessel wall. In all the experimental animals designed for different implantation periods during IBS scaffold R&D process, either rabbits or pigs, no puncture of the vessel wall was found. For the

animals in MR evaluation, no puncture was observed after the onset of backbone iron corrosion after MR examination. Based on the above theoretical analysis and also on the massive *in-vivo* animal data, it can be concluded that fractured scaffold struts accompanied with scaffold degradation would not induce puncture of vessels under MR environment.

Based on the above discussion across the whole life circle of the IBS scaffold, we prudently categorize the brand-new IBS scaffold as MR conditional. MR scanning of patient with implanted IBS scaffolds should be handled with extreme caution. MR examination immediately after IBS implantation is not completely prohibited. However, it is strongly deprecated. If badly needed in specific cases, the procedure should be seriously evaluated before taking actions. If possible, MR examination should be put off after full endothelialization. After full degradation or the best-case full resorption of IBS, MR scanning can be freely performed.

4.2. Similarity and difference among various bioresorbable scaffolds and permanent stents under MR examination

Irrespective of the inherent properties of scaffold/stent materials, the biggest difference between permanent stents and biodegradable/bioresorbable scaffolds is that MR imaging properties of bioresorbable scaffolds will change along with scaffold degradation/resorption. MR scanning of biodegradable scaffolds should be distinctively treated considering the degradation progress of the scaffold. Eventually, no restriction remains for MR examination after full resorption of the scaffold. Fig. 9 displays the MR image artifacts of different scaffolds/
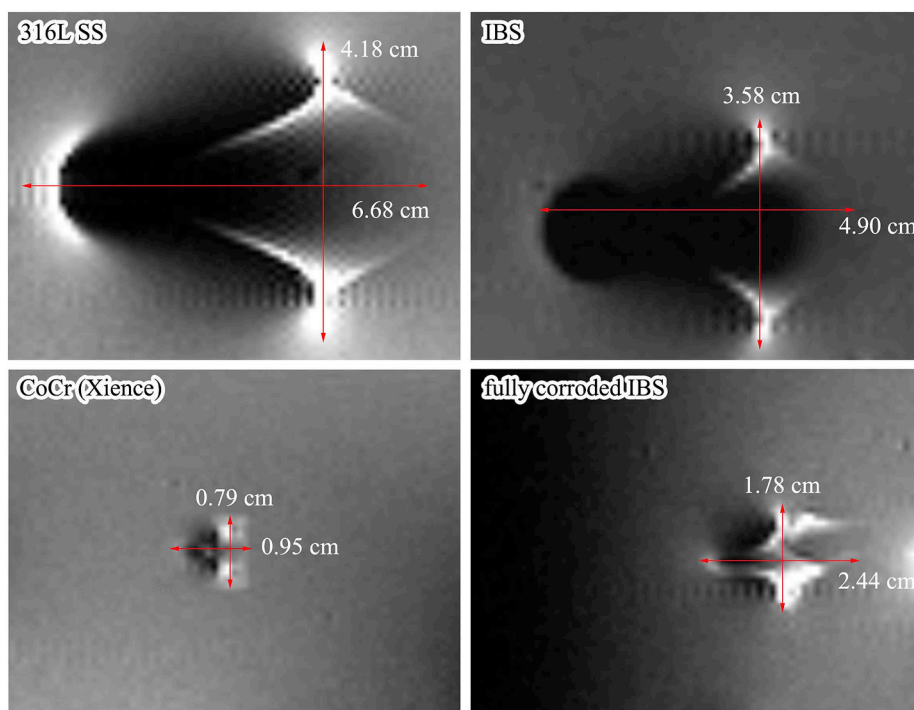
Fig. 9. MR image artifacts comparison of different scaffolds/stents (same specifications, 30015) composed of different backbone materials, including one 316L SS bare stent, one IBS scaffold, one CoCr DES (Xience), and one fully corroded IBS scaffold (nitrided iron backbone weight loss ~100%), pattern of the 316L SS bare stent was the same as the tested IBS scaffold.

stents (with the same specification-30015) composed of different backbone materials, including one 316L SS bare stent, one IBS scaffold, one CoCr DES (Xience), and one fully corroded IBS scaffold (nitrided iron backbone weight loss ~100%). At the original state, MR image artifact of the IBS scaffold was similar to that of 316L SS bare stent, besides, the artifact width of the former was even smaller. However, the artifact area of IBS scaffold was apparently larger than that of the Xience DES (CoCr) counterpart. After full corrosion of IBS, the extent of MR image artifact was dramatically weakened, but it was still a little severe than that of Xience DES. Ferromagnetic Fe_3O_4 was found in the corrosion products, and that's why the small artifacts still existed after full degradation of the nitrided iron backbone. Corrosion products of iron could be gradually cleared away by macrophages [13], therefore it is reasonable to conclude that the remaining MR image artifacts might disappear after full resorption of the corrosion products.

Bioresorbable scaffolds can be roughly divided into two categories, namely the bioresorbable polymeric scaffold and the bioresorbable metallic scaffold, considering their backbone materials. For bioresorbable scaffolds made from polymeric materials, MR scanning could be freely and safely performed at any time after implantation on condition that RF heating is tolerable, since polymeric materials and their degradation products are generally nonmagnetic. They would not pose hazards to the patient. However, for patient implanted with bioresorbable metallic devices, a detailed and well-considered assessment should be needed before performing MR examination, considering the magnetic properties of component materials. Differences among the Mg-based, Zn-based and Fe-based scaffolds under MR environment will be discussed here.

Magnesium is a paramagnetic element, and zinc is a diamagnetic element. Both elements are nonmagnetic. MR safety of Mg-based and Zn-based scaffolds should not be a concern. However, MR image artifacts still exist due to their metallic nature. Artifacts near metallic implants arise from local magnetic field inhomogeneity, which is caused by differences between the magnetic properties of human tissue and those of the implant. The more substantial the difference in magnetic susceptibilities between the metallic object and the surrounding tissue is, the more severe are the resulting artifacts. As opposed to Fe, Mg and

Zn both have much closer magnetic susceptibilities to human tissues, and therefore cause only minor artifacts under MR scanning. In the previous study of a commercial Mg-based compression screw (MAGN-EZIX®, Syntellix AG, Germany), MR image artifacts generated by the magnesium screw had a lesser extent and were less severe as compared to the titanium screw [41,42]. Possible corrosion products of Mg and Zn are their corresponding oxides, hydroxides, carbonates (hydrated carbonates) and phosphates (hydrated phosphates) [36,43]. All of those degradation products are nonmagnetic, so no extra concerns under MR will arise during Mg/Zn scaffold degradation. When magnetic elements, especially for iron, cobalt and nickel, are added into biodegradable scaffolds, their magnetic properties and MR safety & compatibility should be carefully evaluated.

According to the American Heart Association (AHA) Scientific Statement on "Safety of Magnetic Resonance Imaging in Patients with Cardiovascular Devices", coronary stents, including drug-eluting ones, that are nonferromagnetic can be safely scanned at fields of ≤3 T any time after implantation. MR examination can be performed immediately after stent implantation at ≤3 T in patients with peripheral stents that are nonferromagnetic. For peripheral stents with weak ferromagnetism, the timing of MR examination at ≤3 T should be determined on a case-by-case basis. For case in which the patient is with a chronic condition, there is little difference whether the MR scanning is performed immediately after stent implantation or several weeks later. In this situation, MR examination to be performed 6 weeks after stent implantation is recommended. For cases in which there are clear benefits that the MR examination will outweigh the risks of the examination, the MR examination should be carefully performed on the basis that the case is compressively evaluated [31]. Up to now, no recommendations or guidelines have been proposed for MR scanning of bioresorbable scaffolds. When referring to the guidelines for permanent stents, the MR imaging in patients with bioresorbable scaffold should be determined on a case-by-case basis at the same time. MR scanning of patient with bioresorbable scaffolds should be distinctively evaluated with extreme caution, considering the aspects of scaffold itself, patient condition, scaffold deployment and apposition condition, degradation period, properties of potential corrosion products, etc.
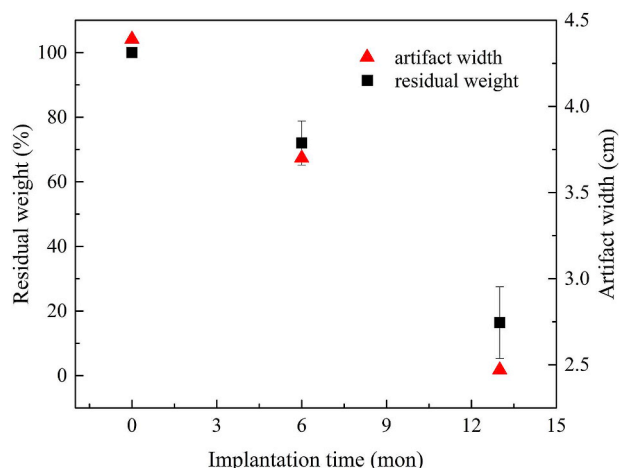
Fig. 10. The correspondence between explant MR artifact width and implant (backbone) weight loss.

4.3. Degradation characterization of magnetic scaffold by using MRI?

Preclinical animal study will be performed to learn the *in-vivo* degradation behaviors of bioresorbable scaffolds before they are implanted into patients. Animal amount is strictly restricted from the ethical perspective. The minimum animals should be used to gain the maximum *in-vivo* data. Normally, intravascular ultrasound (IVUS) and optical coherence tomography (OCT) are used to intravitally characterize the scaffold degradation progress. After the sacrifice of animals, micro-CT is usually performed. IVUS and OCT are all based on interventional operation. Besides, radioactive contrast agent is needed during OCT imaging. In clinical study, IVUS and OCT are normally used to characterize the in-patient scaffold degradation. The frequency to perform IVUS or OCT examination should be strictly controlled, since those two follow-up approaches are based on percutaneous transluminal angioplasty (PTA) and they do harms to the patient.

In-vivo MR evaluation of IBS scaffolds in rabbits revealed that the MR image artifacts decreases as degradation continues. Measurement of the artifact evolution might be a new approach to evaluate the whole-period degradation behaviors of this scaffold [11]. For example, the artifact width/volumes during different degradation periods could be measured in animal models. A corresponding relationship between the artifact width/volume (MR scanning) and scaffold mass (weight loss measurement) or remaining scaffold volume (micro-CT analysis) could be built, as shown in Fig. 10. Then, quantification of the scaffold degradation might be measured through MR scanning after endothelialization. By doing so, the whole lifecycle degradation behavior of an IBS scaffold can be gradually measured in one animal, and therefore a plenty of experimental animals could be saved. For clinical study, the in-man degradation profile could be analogized based on in-animal correspondence simply through MR scanning. That would be a patient-friendly follow-up approach for characterization of scaffold degradation and resorption, as there is no more need for interventional treatment, angiography or contrast agent. However, back to the present, this is only a concept or a guesswork, and there's still a lot to be explored. On all accounts, patient safety comes first.

5. Conclusions

A safe MR scanning for a patient with cardiovascular or peripheral implants involves an accurate determination of the implanted devices and its properties (metallic, magnetic, bioresorbable, etc.), a thoughtful analysis of the benefits and risks of the examination, the proper time to perform the examination, and, when indicated, appropriate physician supervision.

Based on well-designed experiments (*in-vitro*, *ex-vivo* and *in-vivo*) and on a scientifically based rationale, a conclusion can be drawn that the innovative IBS scaffold is MR conditional ($\leq$3T, 2.0 W/kg), though not MR compatible in image artifacts. Even though MR examination immediately after IBS implantation is not completely prohibited, it is strongly not recommended. The MR scanning should be put off after full endothelialization, and no MR constraints remain after full resorption of the IBS scaffold. The systematic methodology used for MR safety & compatibility evaluation in the present study can be applied to other magnetic scaffolds (bioresorbable) or stents (permanent).

CRediT authorship contribution statement

Dong Bian: Methodology, Software, Validation, Formal analysis, Data curation, Visualization, Conceptualization, Writing - original draft, Writing - review & editing. **Li Qin:** Methodology, Software, Validation, Formal analysis, Data curation, Visualization, Conceptualization, Writing - original draft, Writing - review & editing. **Wenjiao Lin:** Methodology, Software, Validation, Formal analysis, Data curation, Visualization, Conceptualization, Writing - original draft, Writing - review & editing. **Danni Shen:** Writing - original draft, Writing - review & editing. **Haiping Qi:** Methodology, Software, Validation, Formal analysis, Data curation, Visualization, Conceptualization, Writing - original draft, Writing - review & editing. **Xiaoli Shi:** Formal analysis. **Gui Zhang:** Methodology, Investigation. **Hongwei Liu:** Methodology, Investigation. **Han Yang:** Methodology, Investigation. **Jin Wang:** Formal analysis. **Deyuan Zhang:** Project administration, Resources, Supervision, Validation, Conceptualization, Writing - review & editing. **Yufeng Zheng:** Supervision, Writing - review & editing.

Declaration of competing interest

The authors declared no conflict of interest.

Acknowledgements

References

[1] S. Garg, P.W. Serruys, Coronary stents: looking forward, J. Am. Coll. Cardiol. 56 (10) (2010) S43–S78.

[2] Y.F. Zheng, X.N. Gu, F. Witte, Biodegradable metals, Math. Sci. Eng. R 77 (2014) 1–34 0.

[3] C. Indolfi, S.D. Rosa, A. Colombo, Bioresorbable vascular scaffolds - basic concepts and clinical outcome, Nat. Rev. Cardiol. 13 (12) (2016) 719–729.

[4] P.W.J.C. Serruys, Y. Onuma, Bioresorbable Scaffolds: from Basic Concept to Clinical Applications, CRC Press, 2017.

[5] Y.Q. Zhu, K. Yang, R.Y. Cheng, Y. Xiang, T.W. Yuan, Y.S. Cheng, B. Sarmento, W.G. Cui, The current status of biodegradable stent to treat benign luminal disease, Mater. Today 20 (9) (2017) 516–529.

[6] H. Jinnouchi, S. Torii, A. Sakamoto, F.D. Kolodgie, R. Virmani, A.V. Finn, Fully bioresorbable vascular scaffolds: lessons learned and future directions, Nat. Rev. Cardiol. 16 (5) (2019) 286–304.

[7] H.S. Han, S. Loffredo, I. Jun, J. Edwards, Y.C. Kim, H.K. Seok, F. Witte, D. Mantovani, S. Glyn-Jones, Current status and outlook on the clinical translation of biodegradable metals, Mater. Today 23 (2019) 57–71.

[8] S.H. Im, Y. Jung, S.H. Kim, Current status and future direction of biodegradable metallic and polymeric vascular scaffolds for next-generation stents, Acta Biomater. 60 (2017) 3–22.

[9] B. Xu, K.F. Dou, R.L. Gao, Iron Based BRS: Design Features, Experimental Studies and FIM Experience, (2018) TCT2018.

[10] W.J. Lin, G. Zhang, P. Cao, D.Y. Zhang, Y.F. Zheng, R.X. Wu, L. Qin, G.Q. Wang, T.Y. Wen, Cytotoxicity and its test methodology for a bioabsorbable nitrided iron stent, J. Biomed. Mater. Res. B 103 (4) (2014) 764–776.

[11] W.J. Lin, D.Y. Zhang, G. Zhang, H.T. Sun, H.P. Qi, L.P. Chen, Z.Q. Liu, R.L. Gao, W. Zheng, Design and characterization of a novel biocorrodible iron-based drug-eluting coronary scaffold, Mater. Des. 91 (2016) 72–79.

[12] S.M. Li, S. McCarthy, Further investigation on the hydrolytic degradation of poly (DL-lactide), Biomaterials 20 (1) (1999) 35–44.

[13] W.J. Lin, L. Qin, H.P. Qi, D.Y. Zhang, G. Zhang, R.L. Gao, H. Qiu, Y. Xia, P. Cao, X. Wang, W. Zheng, Long-term in vivo corrosion behavior, biocompatibility and bioresorption mechanism of a bioresorbable nitrided iron scaffold, Acta Biomater. 54 (2017) 454–468.

[14] Q.M. Feng, D.Y. Zhang, C.H. Xin, X.D. Liu, W.J. Lin, W.Q. Zhang, S. Chen, K. Sun, Characterization and in vivo evaluation of a bio-corrodible nitrided iron stent, J. Mater. Sci. Mater. Med. 24 (3) (2013) 713–724.

[15] T. Karamitsos, S. Neubauer, Cardiovascular magnetic resonance imaging, Medicine 38 (7) (2010) 384–389.

[16] R.I. Pettigrew, Dynamic magnetic resonance imaging in acquired heart disease, Semin. Ultrasound CT MR 12 (1) (1991) 61–91.

[17] J. Hug, E. Nagel, A. Bornstedt, B. Schnackenburg, H. Oswald, E. Fleck, Coronary arterial stents: safety and artifacts during MR imaging, Radiology 216 (2000) 781–787.

[18] J. Schenck, The role of magnetic susceptibility in magnetic resonance imaging: MRI magnetic compatibility of the first and second kinds, Med. Phys. 23 (6) (1996) 815–850.

[19] P. Stradiotti, A. Curti, G. Castellazzi, A. Zerbi, Metal-related artifacts in in-strumented spine. Techniques for reducing artifacts in CT and MRI: state of the art, Eur. Spine J. 18 (1) (2009) 102–108.

[20] F.G. Shellock, J.V. Crues, MR procedures: biologic effects, safety, and patient care, Radiology 232 (3) (2004) 635–652.

[21] V.P.B. Grover, J.M. Tognarelli, M.M.E. Crossey, I.J. Cox, S.D. Taylor-Robinson, M.J.W. McPhail, Magnetic resonance imaging: principles and techniques: lessons for clinicians, J. Clin. Exp. Hepatol. 5 (3) (2015) 246–255.

[22] I.B. Akca, F. Onur, C.J. Yeung, G. Sevin, T. Onur, A. Ergin, Measuring local RF heating in MRI: simulating perfusion in a perfusionless phantom, J. Magn. Reson. Imag. 26 (5) (2010) 1228–1235.

[23] N. Peter, F. Florian, W. Ingo, W. Marcus, M.T. Friedrich, E. Philipp, G. Wolfgang, R. Oliver, P.M. Jakob, M.E. Ladd, Spatial distribution of RF-induced E-fields and implant heating in MRI, Magn. Reson. Med. 60 (2) (2010) 312–319.

[24] J.C. McGowan, Basic principles of magnetic resonance imaging, Neuroimaging Clin. 18 (4) (2008) 623–636.

[25] M. Hui, Chapter 20: basic principles of magnetic resonance imaging, in: X.Y. Chen (Ed.), Molecular Imaging Probes for Cancer Research, World Scientific, 2012, pp. 581–609.

[26] ISO 25539-2:2012(E), Cardiovascular Implants — Endovascular Devices — Part 2: Vascular Stents, second ed., (2012).

[27] ASTM F20525-15, Standard Test Method for Measurement of Magnetically Induced Displacement Force on Medical Devices in the Magnetic Resonance Environment, edition, (2015).

[28] ASTM F2213-17, Standard Test Method for Measurement of Magnetically Induced Torque on Medical Devices in the Magnetic Resonance Environment, (2017).

[29] ASTM F2182-11a, Standard Test Method for Measurement of Radio Frequency Induced Heating on or Near Passive Implants during Magnetic Resonance Imaging, (2011).

[30] ASTM F2119-07, Standard Test Method for Evaluation of MR Image Artifacts from Passive Implants, (2013) reapproved.

[31] G.N. Levine, A.S. Gomes, A.E. Arai, D.A. Bluemke, S.D. Flamm, E. Kanal, W.J. Manning, E.T. Martin, J.M. Smith, N. Wilke, Safety of magnetic resonance imaging in patients with cardiovascular devices: an American heart association scientific statement from the committee on diagnostic and interventional cardiac catheterization, council on clinical cardiology, and the council on cardiovascular radiology and intervention, Circulation 116 (24) (2007) 2878–2891.

[32] J.F. Zheng, H. Qiu, Y. Tian, X.Y. Hu, T. Luo, C. Wu, Y. Tian, Y. Tang, L.F. Song, L. Li, L. Xu, B. Xu, R.L. Gao, Preclinical evaluation of a novel sirolimus-eluting iron bioresorbable coronary scaffold in porcine coronary artery at 6 months, JACC Cardiovasc. Interv. 12 (3) (2019) 245–255.

[33] S.H. Lu, Y.T. Dai, Normal body temperature and the effects of age, sex, ambient temperature and body mass index on normal oral temperature: a prospective, comparative study, Int. J. Nurs. Stud. 46 (5) (2009) 661–668.

[34] K.M. Gupta, N. Gupta, Magnetic materials: properties and behaviour, in: K.M. Gupta, N. Gupta (Eds.), Advanced Electrical and Electronics Materials, John Wiley & Sons, Inc., 2015, pp. 379–421.

[35] F.L. Jin, R.R. Hu, S.J. Park, Improvement of thermal behaviors of biodegradable poly(lactic acid) polymer: a review, Compos. B Eng. 164 (2019) 287–296.

[36] H.T. Yang, C. Wang, C.Q. Liu, H.W. Chen, Y.F. Wu, J.T. Han, Z.C. Jia, W.J. Lin, D.Y. Zhang, W.T. Li, W. Yuan, H. Guo, H.F. Li, G.X. Yang, D.L. Kong, D.H. Zhu, K. Takashima, L.Q. Ruan, J.F. Nie, X. Li, Y.F. Zheng, Evolution of the degradation mechanism of pure zinc stent in the one-year study of rabbit abdominal aorta model, Biomaterials 145 (Supplement C) (2017) 92–105.

[37] R. Virmani, H. Jinnouchi, A.V. Finn, Discontinuity: is it a major cause of scaffold thrombosis? J. Am. Coll. Cardiol. 70 (19) (2017) 2345–2348.

[38] H. Yano, S. Horinaka, T. Ishimitsu, Serial OCT imaging in vascular healing after everolimus-eluting stent implantation, JACC-Cardiovasc, JACC Cardiovasc. Interv. 11 (1) (2018) 147–148.

[39] H.M. Garcia-Garcia, M. Haude, K. Kuku, A. Hideo-Kajita, H. Ince, A. Abizaid, R. Tölg, P.A. Lemos, C. von Birgelen, E.H. Christiansen, W. Wijns, J. Escaned, J. Dijkstra, R. Waksman, In vivo serial invasive imaging of the second-generation drug-eluting absorbable metal scaffold (Magmaris — DREAMS 2G) in de novo coronary lesions: insights from the BIOSOLVE-II First-In-Man trial, Int. J. Cardiol. 255 (2018) 22–28.

[40] E. Tenekecioglu, P.W. Serruys, Y. Onuma, R. Costa, D. Chamié, Y. Sotomi, T.-B. Yu, A. Abizaid, H.-B. Liew, T. Santoso, Randomized comparison of Absorb bioresorbable vascular scaffold and Mirage microfiber sirolimus-eluting scaffold using multi-modality imaging, JACC Cardiovasc. Interv. 10 (11) (2017) 1115–1130.

[41] L. Sonnow, S. Könneker, P.M. Vogt, F. Wacker, C.V. Falck, Biodegradable magne-sium Herbert screw – image quality and artifacts with radiography, CT and MRI, BMC Med. Imag. 17 (1) (2017) 16.

[42] C. Plaass, F.C. Von, S. Ettinger, L. Sonnow, F. Calderone, A. Weizbauer, J. Reifenrath, L. Claassen, H. Waizy, K. Daniilidis, Bioabsorbable magnesium versus standard titanium compression screws for fixation of distal metatarsal osteotomies - 3 year results of a randomized clinical trial, J. Orthop. Sci. 23 (2) (2017) 321–327.

[43] J.W. Lee, H.S. Han, K.J. Han, J. Park, H. Jeon, M.R. Ok, H.K. Seok, J.P. Ahn, K.E. Lee, D.H. Lee, Long-term clinical study and multiscale analysis of in vivo biodegradation mechanism of Mg alloy, Proc. Natl. Acad. Sci. U.S.A. 113 (3) (2016) 716.

[44] F2503-13, Standard Practice for Marking Medical Devices and Other Items for Safety in the Magnetic Resonance Environment, (2013).